



UNIVERSITY OF LEEDS

This is a repository copy of *Self-consistent scattering theory of transport and output characteristics of quantum cascade lasers* .

White Rose Research Online URL for this paper:
<http://eprints.whiterose.ac.uk/1686/>

Article:

Indjin, D., Harrison, P., Kelsall, R.W. et al. (1 more author) (2002) Self-consistent scattering theory of transport and output characteristics of quantum cascade lasers. *Journal of Applied Physics*, 91 (11). pp. 9019-9026. ISSN 1089-7550

<https://doi.org/10.1063/1.1474613>

Reuse

See Attached

Takedown

If you consider content in White Rose Research Online to be in breach of UK law, please notify us by emailing eprints@whiterose.ac.uk including the URL of the record and the reason for the withdrawal request.



eprints@whiterose.ac.uk
<https://eprints.whiterose.ac.uk/>

Self-consistent scattering theory of transport and output characteristics of quantum cascade lasers

D. Indjin,^{a)} P. Harrison, R. W. Kelsall, and Z. Ikonjic
*Institute of Microwaves and Photonics, School of Electronic and Electrical Engineering,
University of Leeds, Leeds LS2 9JT, United Kingdom*

(Received 26 November 2001; accepted for publication 6 March 2002)

Electron transport in GaAs/AlGaAs quantum cascade lasers operating in midinfrared is calculated self-consistently using an intersubband scattering model. Subband populations and carrier transition rates are calculated and all relevant electron-LO phonon and electron-electron scatterings between injector/collector, active region, and continuum resonance levels are included. The calculated carrier lifetimes and subband populations are then used to evaluate scattering current densities, injection efficiencies, and carrier backflow into the active region for a range of operating temperatures. From the calculated modal gain versus total current density dependencies the output characteristics, in particular the gain coefficient and threshold current, are extracted. For the original GaAs/Al_{0.33}Ga_{0.67}As quantum cascade structure [C. Sirtori *et al.*, Appl. Phys. Lett. **73**, 3486 (1998)] these are found to be $g = 11.3$ cm/kA and $J_{\text{th}} = 6 \pm 1$ kA/cm² (at $T = 77$ K), and $g = 7.9$ cm/kA and $J_{\text{th}} = 10 \pm 1$ kA/cm² (at $T = 200$ K), in good agreement with the experiment. Calculations shows that threshold cannot be achieved in this structure at $T = 300$ K, due to the small gain coefficient and the gain saturation effect, also in agreement with experimental findings. The model thus promises to be a powerful tool for the prediction and optimization of new, improved quantum cascade structures.

© 2002 American Institute of Physics. [DOI: 10.1063/1.1474613]

I. INTRODUCTION

A considerable advance has recently been made in the development and optimization of quantum cascade lasers (QCLs).^{1,2} In these complex multilayer structures coherent midinfrared light amplification is achieved via an electronic cascade along the energy level staircase in a sequence of active region and injector/collector multiquantum well structures. QCLs have traditionally been based on InGaAs/AlInAs structure so that growth could be lattice matched to an InP substrate.^{3,4} Based on similar design criteria, more recent designs have been realized in GaAs/AlGaAs structures.⁵ This latter system has attracted attention due to the possibility of low-loss AlGaAs waveguide designs.⁶ The midinfrared GaAs/AlGaAs QCLs have not yet achieved the temperature range of InGaAs/AlInAs devices, but a lot of successful experimental work is currently under way to extend the operating temperature.⁷⁻¹³ On the other hand, GaAs/AlGaAs cascade structures may play an important role in producing stimulated radiation in the far-infrared region, which is also the topic of recent investigations, both experimental¹⁴⁻¹⁶ and theoretical.^{17,18}

The rapid experimental development has stimulated interest in theoretical work to explain the physical processes involved,¹⁹⁻²¹ including the principles of carrier transport in devices, and hence, indicate routes to optimized layer design for improved output characteristics. Theoretical studies to date have mainly addressed the optimization of the active region structure and the electron-LO phonon scattering rates, so as to maximize the population inversion.²²⁻²⁴ The thermalization of the electron distribution function was also

investigated.^{25,26} Most recently, in a theoretical analysis of a QCL, a full injector-active region-collector structure was considered, and it was found that electron-electron scattering plays a crucial role in carrier transfer between injector/collector and active regions of the structure, and is very important in calculations of the population inversion and gain.²⁷⁻²⁹

In the original GaAs/Al_{0.33}Ga_{0.67}As QCL design it was pointed that the main obstacle in extending the working temperature range is the nonunity injection efficiency from the injector into the upper laser level, due to the thermally induced leakage current into the Γ -derived delocalized continuum-like states. Furthermore, there are mechanisms such as scattering-assisted injection of electrons directly from the injector into the lower laser level, leakage to the collector and backflow to the injector from the upper laser level, as well as backflow from the collector to the lower laser level, all of which deteriorate the population inversion and, hence, the optical gain in the laser structure. Including these effects in theoretical models of QCLs is important in view of a disagreement between the experimentally measured gain coefficient and the calculated gain in the simple three-level model under the unity injection approximation,^{5,30} and should result in better understanding of carrier relaxation transport in cascade structures.

In this article we extend the theoretical model of cascade structures^{18,27} and develop a full self-consistent approach which includes the injector/collector, active region and delocalized (continuum-like) states in a QCL. The aim of this model is to calculate the populations of the active region and the injector/collector subbands, and the carrier transition rates within the structure. All the relevant interaction mechanisms have been included in our simulations, i.e., the intra-

^{a)}Electronic mail: d.indjin@ee.leeds.ac.uk

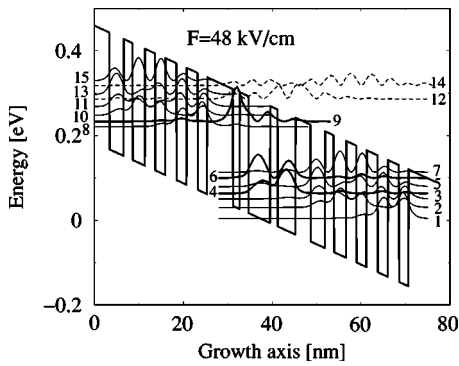


FIG. 1. A schematic diagram of quasibound energy levels and associated wave functions squared for $1\frac{1}{2}$ period (injector-active region-collector) of GaAs/AlGaAs quantum cascade lasers of Ref. 5.

and intersubband electron-LO phonon and electron-electron scattering processes. The results of these calculations can then be used to calculate current densities, injection efficiencies and modal gain, and to estimate the output characteristics, including the gain coefficient and threshold current for a range of temperatures.

II. THEORETICAL CONSIDERATION

As mentioned earlier, full analysis of a QCL requires consideration of the active region, where laser emission takes place, and also of the injector and collector regions. In our notation the collector is, in fact, the injector portion of the next active region in the full cascade scheme. The electronic structure of QCL described in Ref. 5 is illustrated in Figs. 1 and 2. The energy levels of the quasibound states (which correspond to transmission resonances in multilayer quantum structures in an external electric field), were calculated numerically by solving the Schrödinger equation within the effective mass approximation. Nonparabolicity was taken into account,³¹ and the wave functions were obtained via the transfer matrix approach. The injector and collector regions are represented with five energy levels each—subbands 1, 2, 3, 5, and 7 (in the collector) and 8, 10, 11, 13, and 15 (in the

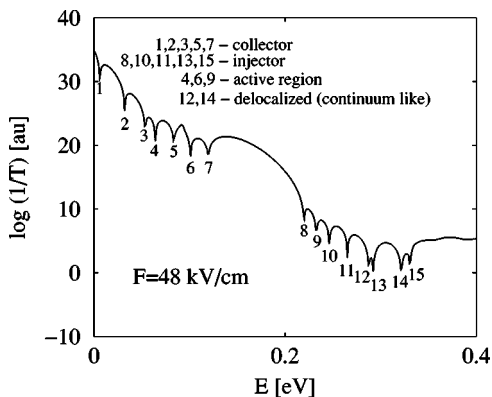


FIG. 2. Calculated transmission of the QCL structure as a function of energy at an applied electric field of $F=48$ kV/cm. The structure studied here had a total of fifteen energy levels (which correspond to transmission resonances): five injector levels, three active region levels, five collector levels, and two weakly localized continuum-like levels.

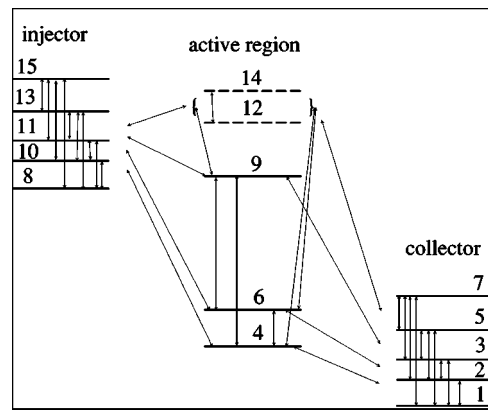


FIG. 3. Carrier transitions in the 15-level system. It is assumed that transitions between the injector and collector regions are negligible.

injector)—in this 15-level model. Radiative transitions occur between the third and second state in the active region, denoted as 9 and 6, while level 4 is the ground state of the active region. There are two additional levels (12 and 14), which correspond to weakly localized (continuum-like) transmission resonances (Fig. 2). Strictly, there are many more delocalized resonances, but for values of the external field around threshold, they are positioned well above the upper injector state and their influence on the carrier dynamics in the structure is negligible.

To introduce periodic boundary conditions, the rate equations were written so that carriers were cycled around the 15-level system. In view of the translation symmetry in our $1\frac{1}{2}$ periods of the full cascade scheme, carriers populate the injector subbands by transfer from the preceding active region and leave the collector subbands to enter the next active region. Scattering transitions between the injector and the preceding active region, as well as those between the collector and the next active region, are characterized equivalently, as scattering inside the central $1\frac{1}{2}$ period of QCL. This approach allows us to close the “scattering circuit” in the rate equation system. The carrier transitions in the structure are shown in Fig. 3. To simplify the calculation the assumption was made that injector subbands were isolated from collector ones; i.e., transition rates between injector and collector regions were negligible. The rate equation for subband 1 is written as

$$\begin{aligned} \frac{dn_1}{dt} = & \frac{n_2}{\tau_{21}} + \frac{n_3}{\tau_{31}} + \frac{n_4}{\tau_{41}} + \frac{n_5}{\tau_{51}} + \frac{n_6}{\tau_{61}} + \frac{n_7}{\tau_{71}} + \frac{n_9}{\tau_{91}} + \frac{n_{(12)}}{\tau_{(12)1}} \\ & + \frac{n_{(14)}}{\tau_{(14)1}} + \frac{n_4}{\tau_{48}} + \frac{n_6}{\tau_{68}} + \frac{n_9}{\tau_{98}} + \frac{n_{(12)}}{\tau_{(12)8}} + \frac{n_{(14)}}{\tau_{(14)8}} - \frac{n_1}{\tau_1}, \end{aligned} \tag{1}$$

where

$$\begin{aligned} (\tau_1)^{-1} = & (\tau_{12})^{-1} + (\tau_{13})^{-1} + (\tau_{14})^{-1} + (\tau_{15})^{-1} + (\tau_{16})^{-1} \\ & + (\tau_{17})^{-1} + (\tau_{19})^{-1} + (\tau_{1(12)})^{-1} + (\tau_{1(14)})^{-1} \\ & + (\tau_{84})^{-1} + (\tau_{86})^{-1} + (\tau_{89})^{-1} + (\tau_{8(12)})^{-1} \\ & + (\tau_{8(14)})^{-1}, \end{aligned}$$

and similarly for other injector and collector states. τ_{if} is a function of both n_i and n_f , the initial and final subband populations. As noted earlier, this injector-active region-collector model must reflect the full periodic cascade structure, and hence, subband 1 must be equivalent to subband 8, and similarly: $2 \rightarrow 10$, $3 \rightarrow 11$, $5 \rightarrow 13$, and $7 \rightarrow 15$. Back-scattering into subband 1 from the next active region is equivalent to the backscattering from the active region subbands 4, 6, and 9 and weakly localized states 12 and 14, into its equivalent subband 8, which is described by the last five terms in the sum in Eq. (1). The equations describing the rates dn_i/dt in the collector region ($i=1,2,3,5,7$) are symmetric with those in the injector region ($i=8,10,11,13,15$), and when the system reaches a steady state, the collector subbands population *should* equal those in injector subband. This implies that the injection rates on each side of the active region are equal.

The rate equation for active region subband 4 is given by

$$\frac{dn_4}{dt} = \sum_{i=1, i \neq 4}^{15} \frac{n_i}{\tau_{i4}} - n_4 \sum_{i=1, i \neq 4}^{15} \frac{1}{\tau_{4i}} \quad (2)$$

and similarly for the other active region subbands, and for the weakly localized subbands 12 and 14. At equilibrium all the rates (dn_i/dt) equal zero. Thus, we have a set of 15 equations which specify the population of each subband in terms of the populations of all the other subbands and the scattering rates between them (which in turn depend on subband populations themselves). Therefore, these 15 equations must be solved self-consistently using an iterative procedure. With an initial guess of subband populations n_i , all the scattering times τ_{if} are calculated and then the next, better approximation to n_i is found. The scattering times are then recalculated on the basis of these subband populations, and the procedure is repeated until self-consistency is reached; i.e., the estimate for n_i is sufficiently close to that of the previous iteration. As usual in self-consistent procedures, to improve the convergence the estimate of subband populations in the next step is supplied by combining the old and new calculated value

$$n_i^{\text{new}} = \xi n_i^{\text{new}} + (1 - \xi) n_i^{\text{old}}, \quad (3)$$

where ξ is a weighting parameter. In our calculations a fixed value of $\xi=0.5$ gives reasonably good convergence for a range of densities and temperatures, though dynamically changing it can lead to improved convergence, particularly at lower values of electric field. In the course of the iterations, the subband populations are continuously renormalized in order to drive the solution towards satisfying the total carrier density in each period of the structure; i.e., when convergence is reached the sum of subband populations in one period (active region plus collector) is equal to sheet carrier density N_s . At this point $n_1 + n_2 + n_3 + n_4 + n_5 + n_6 + n_7 + n_9 + n_{12} + n_{14} = N_s$, and the injector and the corresponding collector levels have equal populations and carrier lifetimes.

The carrier scattering times τ_{if} were calculated including electron-LO phonon and electron-electron scattering rates. The τ_{if} themselves are scalars which represent the average

lifetime of an electron in respect to scattering between two subbands, each characterized by thermalized Fermi-Dirac distribution.²⁵ For full detail see Ref. 32.

From the self-consistent solution of the QCL rate equations the population inversion $\Delta n_i = n_9 - n_6$ is obtained in the steady-state condition. The modal gain is proportional to the population inversion Δn_i and may be written as^{30,33}

$$G_M = \frac{4\pi e^2}{\epsilon_0 \underline{n}} \frac{\langle z_{96} \rangle^2}{2\gamma_{96} L_p \lambda} \Gamma(n_9 - n_6) \equiv g \Gamma J, \quad (4)$$

where λ is the laser emission wavelength, $2\gamma_{96}$ is the experimental full width of half maxima (FWHM) of the electroluminescence spectrum below threshold, \underline{n} is the mode refractive index, ϵ_0 is the vacuum dielectric permittivity, L_p is the length of one period (injector+active region), Γ is the overlap factor between the optical mode and the core active region of the laser, and $\langle z_{96} \rangle$ is the radiative transition matrix element. If the (quasi) linear dependence under subthreshold conditions between the modal gain G_M and the total current density through the structure J is valid, g is defined as the gain coefficient. In a simple three-level model (active region levels 4, 6, and 9 in our notation), under the assumption that all the electrons are injected from the injector into the upper laser level in the active region (unit injection efficiency), and that all electrons escape the bottom active region level into the collector, the population inversion is proportional to current density J .^{3,4,30}

$$\Delta n_i = \frac{J}{e} \tau_9 \left(1 - \frac{\tau_6}{\tau_{96}} \right) \quad (5)$$

and the gain coefficient g in Eq. (4) has an explicit form. However, this is just a first order approximation. In our model all transitions between the 15 levels are considered, including not only injection from the injector into upper laser level, but also injection via continuum levels and via the lower active region levels. In the same way, electron escaping from the intermediate and upper active region levels directly to the collector is also taken into account.

Changing the bias field modifies the potential experienced by electrons and, hence, the energies and wave functions of quasibound states. Consequently, all the lifetimes and the transition matrix elements change with the field, influencing the self-consistent subband populations (and hence, the gain), and the electric current. To extract the gain coefficient one has to change the electric field (i.e., the applied voltage) and calculate the modal gain and total current density for each value of the field. The gain coefficient g [Eq. (4)] should then be obtained from linear interpolation of $G_M(J)$, because the actually calculated $G_M(J)$ dependence is not strictly linear.

Stationary charge transport through the injector-active region-collector interfaces of QCLs is mainly determined by incoherent-scattering mechanisms,³⁴ while coherent-resonant tunneling gives a very small contribution to the total current density.²⁹ This situation, when both principal scattering mechanisms are included (electron-LO phonon scattering, which is relevant mostly for the electronic cascade within the active region, and electron-electron scattering, which plays an essential role in coupling the nonoverlapping

near resonant states between the injector/collector and the active region), the current density through injector–active region interface is given by

$$J_{IA} = J_{I9} + J_{I6} + J_{I4} + J_{Icont}. \quad (6)$$

Each component of current density J_{Ii} is calculated as the difference between the scattering current from injector levels to the active region level under consideration, and the back-scattering current from active region level to injector levels $J_{Ii} = J_{I \rightarrow i} - J_{i \rightarrow I}$; i.e., for the upper laser level

$$J_{I9} = J_{I \rightarrow 9} - J_{I \leftarrow 9} \\ = e \left[\frac{n_8}{\tau_{89}} + \frac{n_{(10)}}{\tau_{(10)9}} + \frac{n_{(11)}}{\tau_{(11)9}} + \frac{n_{(13)}}{\tau_{(13)9}} + \frac{n_{(15)}}{\tau_{(15)9}} \right] \\ - en_9 \left[\frac{1}{\tau_{98}} + \frac{1}{\tau_{9(10)}} + \frac{1}{\tau_{9(11)}} + \frac{1}{\tau_{9(13)}} + \frac{1}{\tau_{9(15)}} \right] \quad (7)$$

and similarly for the other components in Eq. (6). On the other hand, the current density through the active region–collector interface can be written as

$$J_{AC} = J_{9C} + J_{6C} + J_{4C} + J_{contC}, \quad (8)$$

where the components J_{iC} are calculated as the difference between the scattering current from the active region level to the collector levels, and the backscattering current from the collector levels back to the i th active region level. This gives $J_{iC} = J_{i \rightarrow C} - J_{C \rightarrow i}$, where J_{iC} has an analogous form to that in Eq. (7). The current densities given by Eqs. (6) and (8) should be evaluated by the iterative procedure described above until self-consistency is achieved. At this point the current densities across the different device interfaces should be equal, i.e., $J_{IA} = J_{AC} = J$ (this could also be considered as an indicator of convergence). Finally, by repeating the self-consistent procedure for a range of external fields, the total current density J and the corresponding modal gain G_M can be calculated. Assuming a linear dependence of modal gain on total current, from the slope of the least squares fit of $G_M(J)$ dependence, the gain coefficient g can be estimated. The threshold current density J_{th} has to be found according to the expression $G_M = g\Gamma J_{th} = \alpha_M + \alpha_W$, where α_M and α_W are the mirror and waveguide losses, respectively.

III. NUMERICAL RESULTS AND DISCUSSION

Although the proposed model is quite general and applicable to different cascade structures, the original GaAs/Al_{0.33}Ga_{0.67}As structure described in Ref. 5 was analyzed. The main reason was the fact that a large amount of experimental results have been published^{5,10,11,30} for the structure. Having demonstrated the capability of the model by comparison with this experimental data, it may be readily extended to analyze recent improved designs,^{7–11} and to optimize the design of structures. The layer sequence of one injector–active region period of structure, in nanometers, from left to right starting from the injection barrier is **5.8**/1.5/**2.0**/4.9/**1.7**/4.0/**3.4**/3.2/**2.0**/2.8/**2.3**/2.3/**2.5**/2.3/**2.5**/2.1, where the normal script are wells and bold script barriers. The electron effective mass in the GaAs quantum wells was taken as 0.067 m_0 , and in Al_{0.33}Ga_{0.67}As barriers it is 0.094 m_0 ; the

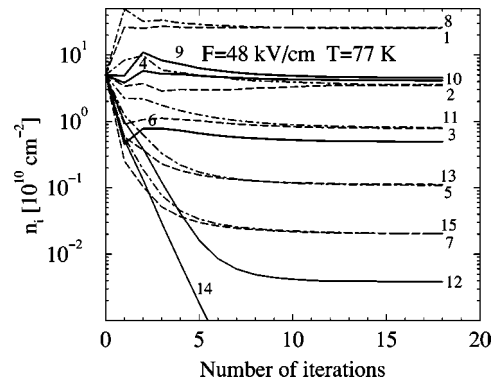


FIG. 4. Subband populations vs number of iterations in the self-consistent calculation, at $T = 77$ K and $F = 48$ kV/cm. Convergence is achieved after 15 iterations when the derivatives of curves tend to zero. At equilibrium, the corresponding injector and collector levels have the same subband populations.

energy gaps were taken as 1.426 and 1.837 eV in the well and barrier layers, respectively; the barrier height was 276 meV. A total carrier density of $N_s = 39 \times 10^{10} \text{ cm}^{-2}$ was derived from the dopant profile per repeat period, and this was assumed, in the first instance, to be distributed evenly between ten subbands in the injector/collector–active region period. The subband populations versus the number of iterations in the self-consistent calculation at the temperature of $T = 77$ K and under the external field of $F = 48$ kV/cm are shown in Fig. 4. Convergence is reached after 15 iterations. At this point the injector and the corresponding collector levels have equal populations, and the sum of populations in one period is strictly equal to N_s . Generally, calculations show that including all electron–LO phonon and electron–electron scatterings in the present 15–level model has a significant effect on subband carrier populations, although substantially increases the CPU time required. The calculated scattering times confirmed the anticipation that electron–LO phonon scattering is dominant in electron transfer between active laser levels, while e–e scattering is essential in low-energy change carrier relaxation inside the injector/collector regions, and also in transfers such as injector levels \rightarrow continuum levels, injector levels \rightarrow upper laser level and lower laser levels \rightarrow collector levels. To reduce the number of iterations in the next self-consistent cycle (i.e., for the next case of temperature or electric field) the final subband populations from the previous loop are used as the next initial guess. For example, Fig. 5 shows that, for $T = 300$ K and $F = 55$ kV/cm, convergence is achieved after ten iterations. At low temperature (Fig. 4) the populations of the second injector state (level 10) and the upper laser state (level 9) become very similar due to a good level alignment. At the same time, subband populations of lower laser levels (6 and 4) are larger than those of the corresponding levels in the collector region due to rapid low-temperature relaxation in collector. In contrast, at the highest temperature (Fig. 5) the thermalization of carriers in the injector/collector region makes the subband populations of levels 3(11) and 7(15) become equal to those in the active region levels 4 and 6, respectively.

The temperature dependence of the subband populations in the active region is shown in Fig. 6 for three different

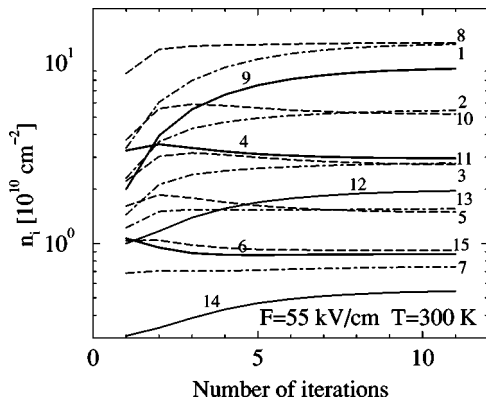


FIG. 5. Same as in Fig. 4 but at $T=300$ K, $F=55$ kV/cm and with improved initial conditions. The weighting factor ξ in the self-consistent calculation is dynamically adjusted. Convergence is achieved after ten iterations.

values of electric field. For lower values of field ($F=35$ kV/cm) there is a small population in the upper laser level due to poor level alignment, reduced carrier injection from the injector. For higher fields (around threshold) the population of the upper laser level increases with temperature up to 200 K, followed by a relatively slow decrease for higher temperatures. The population of the lower laser level (level 6) increases with increasing temperature, mainly due to thermally induced backfilling, hence, reducing inversion. The populations of the continuum levels increase with temperature because of thermal broadening of the carrier distribution in the injector levels and the resulting increased energy overlap. This effect is particularly important at higher temperatures and higher fields because such operating conditions open parallel carrier transition channels and cause carrier leakage from the injector into the continuum levels.

The population inversion $\Delta n_i = n_9 - n_6$ as a function of temperature for different values of the applied field, is shown in Fig. 7. The inversion significantly increases with field, mainly due to improved band line-up and electron-electron scattering induced coupling between the populated lowest injector level and the upper laser level. For fields around threshold (≈ 50 kV/cm) the inversion reaches a maximum at around 200 K, with a reduction in inversion observed at higher temperatures, as noted above.

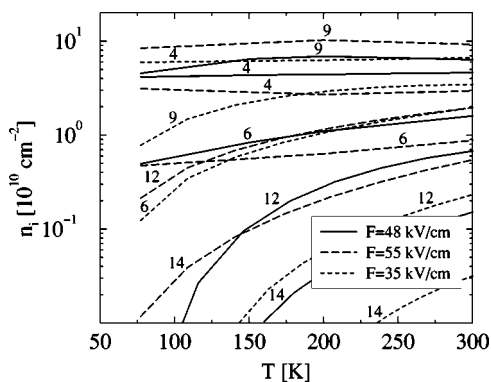


FIG. 6. The subband populations in the active region vs temperature for three values of applied electric field.

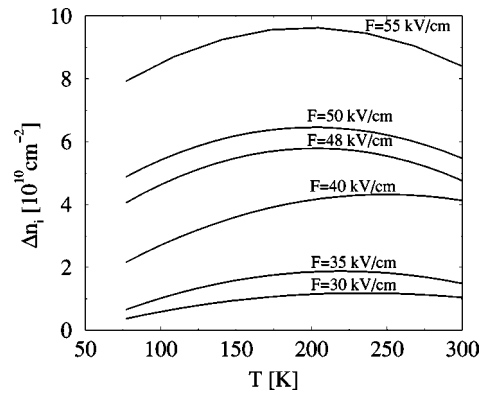


FIG. 7. The population inversion $\Delta n_i = n_9 - n_6$ as a function of temperature for different bias conditions.

Figure 8 shows the dependence of carrier lifetimes in the active and injector/collector levels on temperature, calculated at the point of convergence, for the electric field of $F=48$ kV/cm. The state with the longest lifetime is the lowest energy state in the injector/collector $\tau_1 (= \tau_8)$, which represents the scattering time from the injector level with the highest population into the active region. This time amounts to 3.5 ps at low temperatures and decreases to 0.4 ps at room temperature. The other injector/collector states have fast (subpicosecond) lifetimes, which is important for carrier cooling. The lifetime of the ground active region level τ_4 which is mainly determined by scattering from the active region to the collector also decreases with temperature from 1.2 to 0.3 ps.

Figure 9 shows the lifetimes of active levels, τ_9 and τ_6 , as well as the intersubband scattering time τ_{96} relevant for lasing, for three different values of electric field. Clearly, the lifetimes themselves decrease slowly with temperature. Furthermore, the lasing condition $\tau_{96} > \tau_6$ is clearly satisfied. The fact that the total lifetime τ_9 of the carriers in the upper laser level is significantly less than the scattering time from the upper to the lower laser level τ_{96} , indicates that a substantial fraction of carriers in the upper laser level is lost by being scattered into states outside the active region (into collector levels, or via backfilling the injector levels). It is interesting to note the monotoneous behavior of τ 's with tem-

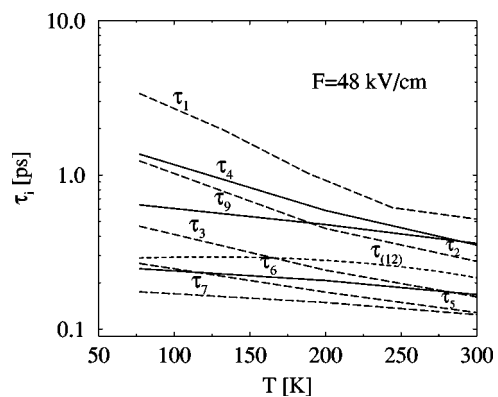


FIG. 8. The carrier lifetimes vs temperature dependence at an applied electric field of $F=48$ kV/cm.

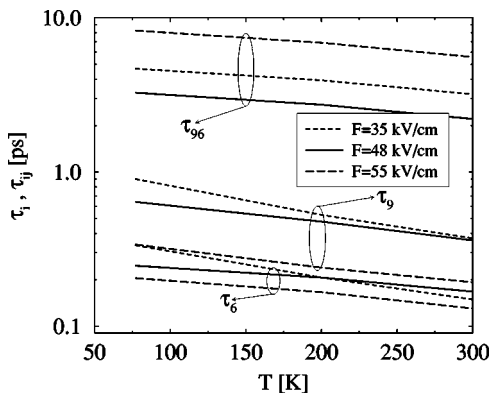


FIG. 9. The intersubband scattering times and total lifetimes of the active laser levels, as these depend on temperature, for different bias conditions.

perature, but nonmonotoneous behavior with the electric field.

The self-consistent calculation of scattering current densities through the structure (for $F = 48$ kV/cm and $T = 77$ K) is shown in Fig. 10. At the point where the iteration procedure starts to converge, total current densities through the injector–active region interface (J_{IA}) and active region–collector interface (J_{AC}) become very similar, tending simultaneously to the full convergence point. About 75% of carriers are then injected from the injector into the upper laser level, 15% into lower laser level and 10% into the active region ground level, while the injection into the continuum states is practically negligible (less than 1%). At the same time, carrier escape from the active region into the collector occurs via the active region ground level–collector states transitions (82%) and lower laser level–collector transitions (9%), while 11% of the carriers escape directly from the upper laser level into the collector. As is well known from the approximate three-level model with nonunity injection,³⁵ the fractional injection rates are very important parameters and significantly affect laser gain. The temperature dependence of the injection efficiency into the active region for different bias values, and also of the escape rates of electrons

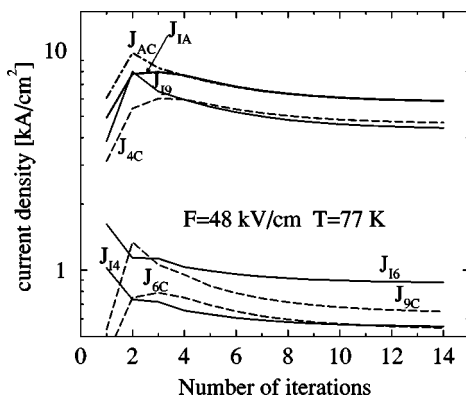


FIG. 10. The scattering current densities through the injector–active region and active region–collector interfaces vs the number of iterations in the self-consistent calculation (at $T = 77$ K and $F = 48$ kV/cm). After four iterations the total current densities through the two interfaces become equal and simultaneously tend to fully converged value.

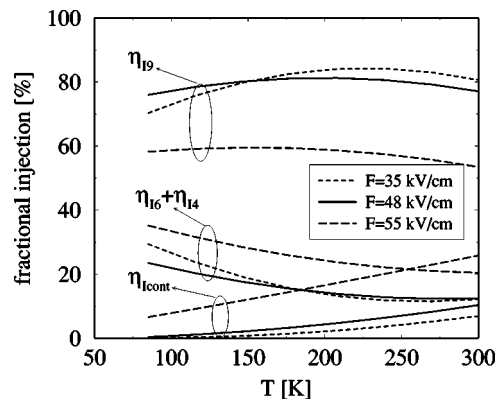


FIG. 11. The injection efficiencies from the injector into the upper laser level (η_{19}), from the injector into the lower active region levels (η_{16} and η_{14}) and from the injector into the continuum levels (η_{cont}), as functions of temperature for three different values of applied electric field.

from the active region into the collector were also investigated, and the results are given in Figs. 11 and 12.

One can see from Fig. 11 that the injection efficiency into the upper level, $\eta_{19} = J_{19}/J$, is only weakly dependent on temperature but significantly decreases with increasing electric field above 55 kV/cm. The latter is because of the increase of injection into lower levels ($\eta_{16} + \eta_{14} = J_{16}/J + J_{14}/J$) and because of the opening of parallel channels (characterized by $\eta_{cont} = J_{cont}/J$) for carrier transfer via continuum resonance levels at higher temperatures. In any case, the decrease of injection into the lower active region levels due to thermalization of electrons in the bottom injector level is compensated (and even overcompensated) by increased injection of thermalized electrons into continuum levels, resulting in injection losses up to 50%, and hence, in gain saturation at high fields (i.e., high current densities).

The fraction of carriers that escape into the collector region is shown in Fig. 12. The sum of the escape current ratios from the lower active region levels into the collector ($\eta_{6C} + \eta_{4C} = J_{6C}/J + J_{4C}/J$) decreases with temperature as a result of an increasing current fraction through the continuum levels ($\eta_{contC} = J_{contC}/J$). The portion of carriers that escape from the upper laser level directly to the collector

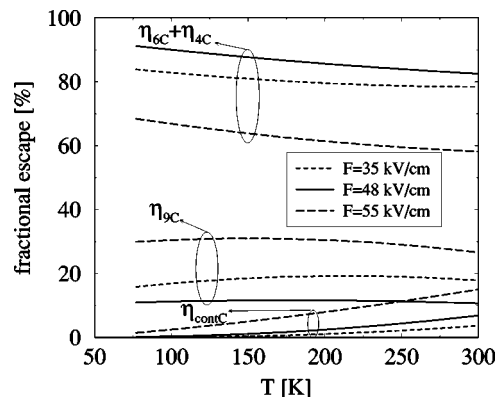


FIG. 12. The fractional escape of carriers from the upper laser level into the collector (η_{9C}), from the lower active region levels into the collector (η_{6C} and η_{4C}), and from the continuum levels into the collector (η_{contC}), as they vary with temperature for three different values of applied electric field.

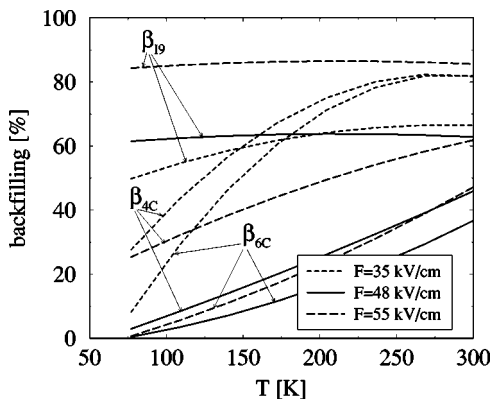


FIG. 13. The backflow of carriers from the upper laser level to the injector (β_{19}), from the collector to the lower laser level (β_{6c}), and from the collector to the ground active region level (β_{4c}) as they vary with temperature for three different values of applied electric field.

(characterized by $\eta_{9c} = J_{9c}/J$), which is an important loss mechanism, increases as the electric field moves away from the optimal value of around 48 kV/cm. This is mostly due to the field induced detuning of the upper laser level energy from the position of minimal quantum mechanical transmission into the collector superlattice region (which is located around the middle of the collector miniband), hence, increasing the wave function overlap between the upper laser level and the collector levels.

For a better understanding of the net current transfer shown earlier, the ratios of carriers backflowing from the upper laser level to the injector ($\beta_{19} = J_{1\leftarrow 9}/J_{1\rightarrow 9}$) and from the collector levels back to the active region ($\beta_{4c} = J_{4\leftarrow c}/J_{4\rightarrow c}$ and $\beta_{6c} = J_{6\leftarrow c}/J_{6\rightarrow c}$) are shown in Fig. 13. Backfilling to the injector is clearly independent of temperature and is relatively strong (60% around threshold) because the injector ground level is slightly below the upper laser level. The increase in β_{19} for higher fields also implies that inversion saturation may occur. On the other hand, backfilling from the collector is temperature dependent due to thermalization of carriers in the collector, and it can also have a strong influence on the reduction of the inversion in the higher temperature-higher field operating regime.

In Fig. 14 the modal gain as a function of current density at 77, 200, and 300 K is given, calculated with the parameter values $\lambda = 9.3 \mu\text{m}$, $\underline{n} = 3.28$, $L_p = 45.3 \text{ nm}$, $2\gamma_{96} = 15 \text{ meV}$ (at $T = 77 \text{ K}$), $2\gamma_{96} = 21 \text{ meV}$ (at $T = 200 \text{ K}$), $2\gamma_{96} = 25 \text{ meV}$ (at $T = 300 \text{ K}$).^{5,10,11,30} Following Eq. (4) we can derive the gain coefficient g by dividing the slope of the linear fit by the overlap factor $\Gamma = 0.42$.^{5,11} We obtain $g = 11.3 \text{ cm/kA}$ at $T = 77 \text{ K}$, $g = 7.9 \text{ cm/kA}$ at $T = 200 \text{ K}$, and $g = 5.4 \text{ cm/kA}$ at $T = 300 \text{ K}$. The gain coefficients are in good agreement with experiment ($g = 8.7 \text{ cm/kA}$ at $T = 77 \text{ K}$ and $g = 6.2 \text{ cm/kA}$ at $T = 200 \text{ K}$),^{5,30} and agree much better than the gain coefficients calculated within the simple three-level model under the unity injection approximation.^{5,30} The expected reduction of the gain coefficient with temperature is due to the various loss mechanisms analyzed earlier, and is also caused by the experimentally established increase of the FWHM. In accordance with the experimentally obtained losses²⁷ $\alpha_M = 6 \text{ cm}^{-1}$ and $\alpha_W = 24 \pm 2 \text{ cm}^{-1}$, from the intersection points of

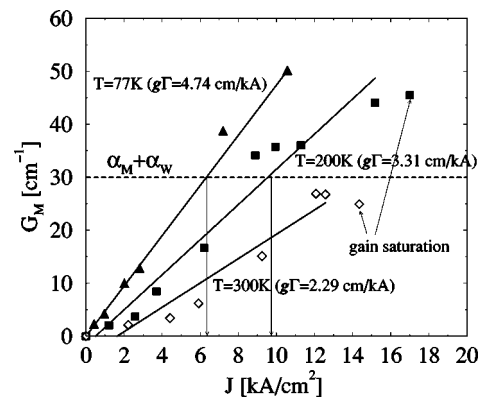


FIG. 14. Calculated modal gain vs the current density dependence for three typical temperatures. The symbols are the calculated data and the solid line represents a least square fit used to derive the values of gain coefficient g . The laser threshold is reached when $G_M(J)$ equals the total loss ($\alpha_M + \alpha_W \approx 30 \text{ cm}^{-1}$ in this example) marked by horizontal dashed line on the graph.

the total loss line $\alpha_M + \alpha_W \approx 30 \text{ cm}^{-1}$ and the $G_M(J)$ lines, we obtain the threshold currents $J_{th} = 6 \pm 1 \text{ kA/cm}^2$ at $T = 77 \text{ K}$ and $J_{th} = 10 \pm 1 \text{ kA/cm}^2$ at $T = 200 \text{ K}$. At lower temperatures the calculated threshold current is in excellent agreement with experiment ($J_{th} = 4 - 7 \text{ kA/cm}^2$),^{5,11,30} while at $T = 200 \text{ K}$ a small discrepancy appears (the lowest experimentally measured value was 12 kA/cm^2).^{10,11,30} Furthermore, the calculation predicts that threshold cannot be achieved in this particular GaAs/Al_{0.33}Ga_{0.67}As structure at $T = 300 \text{ K}$, due to the gain saturation effect, also in agreement with experimental findings.

Finally the calculated electric field-current density characteristics at three operating temperatures is shown in Fig. 15. This translates into the current-voltage characteristics if the series resistance losses, for which there exist some experimental uncertainty, are specified. The calculations are thus in good overall qualitative and quantitative agreement with experiment.

IV. CONCLUSION

A theory of self-consistent scattering transport has been developed, which includes all relevant electron-LO phonon and electron-electron interactions, and the transition rates

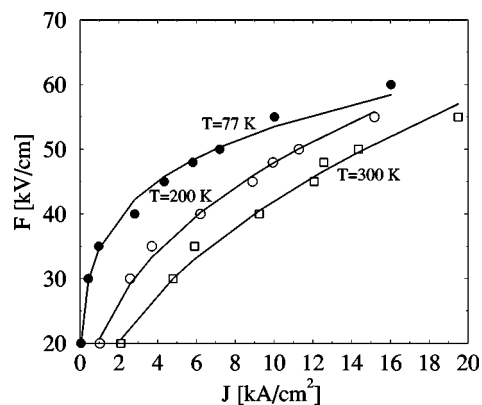


FIG. 15. Electric field vs current density characteristics at $T = 77 \text{ K}$, $T = 200 \text{ K}$, and $T = 300 \text{ K}$.

and subband populations in 15-level model of quantum cascade structure have been calculated. These results were then used to calculate the current densities and injection efficiencies in the active laser region, as well as backflow transport of carriers. The significant influence of current flow via the continuum levels, particularly in the higher temperature/higher bias operating regime is found. Extracted output characteristics, like the gain and threshold currents, are in very good agreement with experiment, and indicate that the proposed model is a very useful numerical technique for attaining better understanding of the physics of quantum cascade lasers as well as for analyzing and optimizing device designs.

ACKNOWLEDGMENT

This work is supported by EPSRC Grant No. GR/R04485.

- ¹J. Faist, F. Capasso, D. L. Sivco, A. L. Hutchison, and A. Y. Cho, *Science* **264**, 553 (1994).
- ²J. Faist, F. Capasso, D. L. Sivco, A. L. Hutchison, C. Sirtori, S. N. G. Chu, and A. Y. Cho, *Appl. Phys. Lett.* **65**, 2901 (1994).
- ³J. Faist, F. Capasso, C. Sirtori, D. L. Sivco, and A. Y. Cho, in *Semiconductors and Semimetals*, edited by H. C. Liu and F. Capasso (Academic, London, 2000), Vol. 66, p. 1, and reference therein.
- ⁴For recent review see, C. Gmachl, F. Capasso, D. L. Sivco, and A. Y. Cho, *Rep. Prog. Phys.* **64**, 1533 (2001).
- ⁵C. Sirtori, P. Kruck, S. Barbieri, P. Collot, J. Nagle, M. Beck, J. Faist, and U. Oesterle, *Appl. Phys. Lett.* **73**, 3486 (1998).
- ⁶C. Sirtori, P. Kruck, S. Barbieri, H. Page, J. Nagle, M. Beck, J. Faist, and U. Oesterle, *Appl. Phys. Lett.* **75**, 3911 (1999).
- ⁷P. Kruck, H. Page, C. Sirtori, S. Barbieri, M. Stellmacher, and J. Nagle, *Appl. Phys. Lett.* **76**, 3340 (2000).
- ⁸C. Becker, C. Sirtori, H. Page, G. Glastre, V. Ortiz, X. Marcadet, M. Stellmacher, and J. Nagle, *Appl. Phys. Lett.* **77**, 463 (2000).
- ⁹S. Barbieri, C. Sirtori, H. Page, M. Stellmacher, and J. Nagle, *Appl. Phys. Lett.* **78**, 282 (2001).
- ¹⁰H. Page, C. Backer, A. Robertson, G. Glastre, V. Ortiz, and C. Sirtori, *Appl. Phys. Lett.* **78**, 3529 (2001).
- ¹¹L. R. Wilson, P. T. Keightley, J. W. Cockburn, M. S. Skolnick, J. C. Clark, R. Grey, and G. Hill, *Appl. Phys. Lett.* **76**, 801 (2000).
- ¹²P. T. Keightley, L. R. Wilson, J. W. Cockburn, M. S. Skolnick, J. C. Clark, R. Grey, G. Hill, and M. Hopkinson, *Physica E (Amsterdam)* **7**, 8 (2000).
- ¹³L. Hvozdar *et al.*, *Appl. Phys. Lett.* **77**, 1241 (2000).
- ¹⁴M. Rochat, J. Faist, M. Beck, U. Oesterle, and M. Illegems, *Appl. Phys. Lett.* **73**, 3724 (1998).
- ¹⁵J. Ulirch, R. Zobl, K. Unterrainer, G. Strasser, and E. Gornik, *Appl. Phys. Lett.* **76**, 19 (1999).
- ¹⁶N. N. Zinov'ev, A. V. Andrainov, V. Yu. Nekrasov, V. A. Petrovskii, L. V. Belyakov, O. M. Sreseli, G. Hill, and J. M. Chamberlain, *JETP Lett.* **74**, 100 (2001).
- ¹⁷K. Donovan, P. Harrison, and R. W. Kelsall, *Appl. Phys. Lett.* **75**, 1999 (1999).
- ¹⁸P. Harrison and R. A. Soref, *IEEE J. Quantum Electron.* **37**, 153 (2001).
- ¹⁹V. B. Gorfinkel, S. Luryi, and B. Gelmot, *IEEE J. Quantum Electron.* **32**, 1995 (1995).
- ²⁰S. Slivken, I. V. Litvinov, and M. Razeghi, *J. Appl. Phys.* **85**, 665 (1999).
- ²¹C. Y. Cheung, P. Rees, and K. A. Shore, *IEE Proc.: Optoelectron.* **146**, 9 (1999).
- ²²K. Donovan, P. Harrison, R. W. Kelsall, and P. Kinsler, *Superlattices Microstruct.* **25**, 373 (1999).
- ²³P. Harrison and R. W. Kelsall, *J. Appl. Phys.* **81**, 7135 (1997).
- ²⁴S. Tomić, M. Tadić, V. Milanović, and Z. Ikonić, *J. Appl. Phys.* **87**, 7965 (2000).
- ²⁵P. Harrison, *Appl. Phys. Lett.* **75**, 2800 (1999).
- ²⁶R. C. Iotti and F. Rossi, *Appl. Phys. Lett.* **76**, 2265 (2000).
- ²⁷K. Donovan, P. Harrison, and R. W. Kelsall, *J. Appl. Phys.* **89**, 3084 (2001).
- ²⁸R. C. Iotti and F. Rossi, *Appl. Phys. Lett.* **78**, 2902 (2001).
- ²⁹R. C. Iotti and F. Rossi, *Phys. Rev. Lett.* **87**, 146603 (2001).
- ³⁰S. Barbieri, C. Sirtori, H. Page, M. Back, J. Faist, and J. Nagle, *IEEE J. Quantum Electron.* **36**, 736 (2000).
- ³¹C. Sirtori, F. Capasso, J. Faist, and S. Scandalo, *Phys. Rev. B* **50**, 8663 (1994).
- ³²P. Harrison, *Quantum Wells, Wires and Dots: Theoretical and Computational Physics* (Wiley, Chichester, 1999).
- ³³G. Sun and J. B. Khurgin, *IEEE J. Quantum Electron.* **29**, 1104 (1993).
- ³⁴C. Sirtori, F. Capasso, J. Faist, A. L. Hutchinson, D. L. Sivco, and A. Y. Cho, *IEEE J. Quantum Electron.* **34**, 1722 (1998).
- ³⁵J. Faist, M. Beck, T. Aellen, and E. Gini, *Appl. Phys. Lett.* **78**, 147 (2001).